

Short Communication

Electrochemical Corrosion Behavior of Ferritic Steels in Molten (Li,Na,K)F

Yanli Wang^{1,*}, Huijun Liu², Chaoliu Zeng², and Weihua Li^{1,*}

¹ School of Chemistry and Chemical Engineering, Guangxi University, Nanning, 530004, P R China.

² Laboratory for Corrosion and Protection, Institute of Metal Research, Chinese Academy of Sciences, 62 Wencui Road, Shenyang 110016, P R China.

*E-mail: wyl15104008565@126.com

Received: 23 October 2017 / Accepted: 2 December 2017 / Published: 28 December 2017

The corrosion of ferritic steels in fluoride salts limits the development of advanced molten salt reactors. In-situ electrochemical measurements for B409M and B439 were performed at 700 °C in molten (Li,Na,K)F by potentiodynamic polarization and electrochemical impedance spectroscopy. The experimental results indicate that the current densities for B409M and B439 are approximately 631 and 738 $\mu\text{A}\cdot\text{cm}^{-2}$, respectively. The impedance spectra plots for B409M and B439 are both composed of two capacitance loops for the duration of a 100 h experimental test. Cr-depleted corrosion layers are formed on the surface of B409M and B439 through fluoridation processes. And the corrosion mechanism is also discussed.

Keywords: Ferritic steel, Corrosion mechanism, Electrochemical, Molten (Li,Na,K)F.

1. INTRODUCTION

Ferritic steels are the main candidates for fusion blankets in nuclear reactors [1-3]. Ferritic steel corrosion in high temperature molten fluoride salts is a key factor that limits the life of advanced molten salt reactors. The eutectic fluoride salts LiF-BeF₂ and (Li,Na,K)F are attractive breeding materials for advanced fusion blanket systems and fusion/fission engines due to their advantageous thermophysical and thermochemical properties at high temperatures [4-10]. However, beryllium containing salts are toxic, expensive to handle and environmentally unfriendly. The molten salt (Li,Na,K)F has some characteristics similar to those of LiF-BeF₂ without the disadvantages caused by beryllium [11]. Therefore, in this work, we use (Li,Na,K)F as the simulator fluid in corrosion tests.

The corrosion characteristics of ferritic steels are mostly researched through weight measurements of the steels in molten fluoride salts [4, 12-18]. Nagasaka [11] examined the corrosion

characteristics of JLF-1 (Fe-9Cr-2W-0.1C) and V-4Cr-4Ti at 873K under static LiF-BeF₂ conditions, and they determined that the mass loss of JLF-1 was approximately 0.15 mg/cm² after 2003 h, which was 10-30 times smaller than the loss of V-4Cr-4Ti. Kondo noted that the corrosion of JLF-1 in molten salts, e.g., LiF-BeF₂ and (Li,Na,K)F was mainly caused by the dissolution of Fe and Cr due to fluoridation and/or electrochemical corrosion [13, 17]. The corrosion of ferritic steels in molten fluorides is intrinsically an electrochemical process [13]. Therefore, in-situ electrochemical measurement techniques can provide valuable insights into the degradation of materials under realistic conditions and allow a better understanding of corrosion mechanisms to be obtained. Limited electrochemical measurements of Fe-based alloys in molten fluorides have been performed [16, 18]. Dasher performed in situ electrochemical impedance spectroscopy measurements on oxide dispersion strengthened (ODS) ferritic steels from 600 °C to 900 °C, and they observed that the ODS steel/coolant interfacial resistance increased with temperature [16]. Therefore, the in-situ electrochemical data available on the chemical compatibility of steels with molten fluoride salts at high temperatures are still limited. In this paper, we attempt to address this deficiency by comparing the in situ electrochemical behaviors of B409M (~ 11.42 wt. % Cr) and B439 (~ 17.30 wt. % Cr) in molten (Li,Na,K)F at 700 °C.

2. EXPERIMENTAL PROCEDURES

The ferritic steels, B409M and B439, were used in the present study, and their chemical compositions are listed in Table 1. The alloy plates were cut into specimens with a size of 5 mm × 30 mm × 2 mm by an electric spark cutting machine, and the specimens were then ground with 1000 grit SiC paper, rinsed with distilled water and then dried. A Fe-Cr wire was spot-welded to one end of the specimens for the electrical connection. The sample was sealed in an alumina tube with high-temperature cement, and a length of 15 mm was exposed. The cement was dried at room temperature for 24 h and then further solidified at 150 °C for 12 h. The exposed surfaces of the specimens were polished again with 1000 grit SiC paper, rinsed and dried prior to testing.

A ternary eutectic mixture, 46.5LiF-11.5NaF-42KF (mole percent) was used for the corrosion study. After drying LiF, NaF and KF, a mixture of (Li,Na,K)F was prepared and placed into a graphite crucible. The mixed fluorides of 178.6 g were further dried at 200 °C in the reaction chamber under vacuum for at least 48 h, and then, the furnace was heated to the experimental temperature of 700 °C.

All the experiments were conducted in a closed, stainless-steel chamber under the protection of pure Ar [19, 20]. The electrochemical measurements, including the potentiodynamic polarization and electrochemical impedance measurements were conducted at 700°C using a Princeton Applied Research PARSTAT 2273 potentiostat/galvanostat system. The potentiodynamic polarization was undertaken performed at a scan rate of 20 mV·min⁻¹, using a conventional three-electrode system with a Pt wire as the reference electrode and a graphite plate as the counter electrode. The electrochemical impedance measurements were carried out between 0.01 Hz and 100 kHz using a two-electrode system (two working electrodes) at the open circuit potential. The amplitude of the input sin wave voltage was 10 mV.

Additionally, the surface and cross-sectional morphologies of the Fe-Cr alloys corroded in molten (Li,Na,K)F for 100 h were also examined by using a scanning electron microscope (SEM) coupled with an energy dispersive X-ray spectrometer (EDX).

Table 1. The composition of the ferritic steels, B409M and B439, used in this study (wt. %).

Alloys	Fe	Cr	C	Si	Mn	P	S	Mo	Ni	N	Nb	Ti
B409M	Bal.	11.42	<0.02	0.50	0.25	0.016	0.002	0.02	0.11	0.0062	0.226	0.193
B439	Bal.	17.30	<0.02	0.58	0.28	0.016	0.001	---	0.13	0.113	0.020	0.182

3. RESULTS AND DISCUSSION

3.1 Potentiodynamic polarization measurement

Fig. 1 presents the potentiodynamic polarization curves of the ferritic steels B409M and B439 in molten (Li,Na,K)F at 700 °C under pure Ar atmosphere, respectively. The ferritic steels are both in active states at the corrosion potential. The corrosion current density (I_{corr}), the corrosion potential (E_{corr}) and the anodic and the cathodic Tafel slopes (b_a and b_c) are calculated by the Tafel extrapolation method, as listed in Table 2. The corrosion potentials of B409M and B439 are approximately -429 and -432 mV vs. Pt, respectively. Moreover, the corrosion current density of B439 with a higher Cr content is about $738 \mu\text{A}\cdot\text{cm}^{-2}$, which is slightly larger than that of the B409M ($631 \mu\text{A}\cdot\text{cm}^{-2}$), which has a lower Cr content.

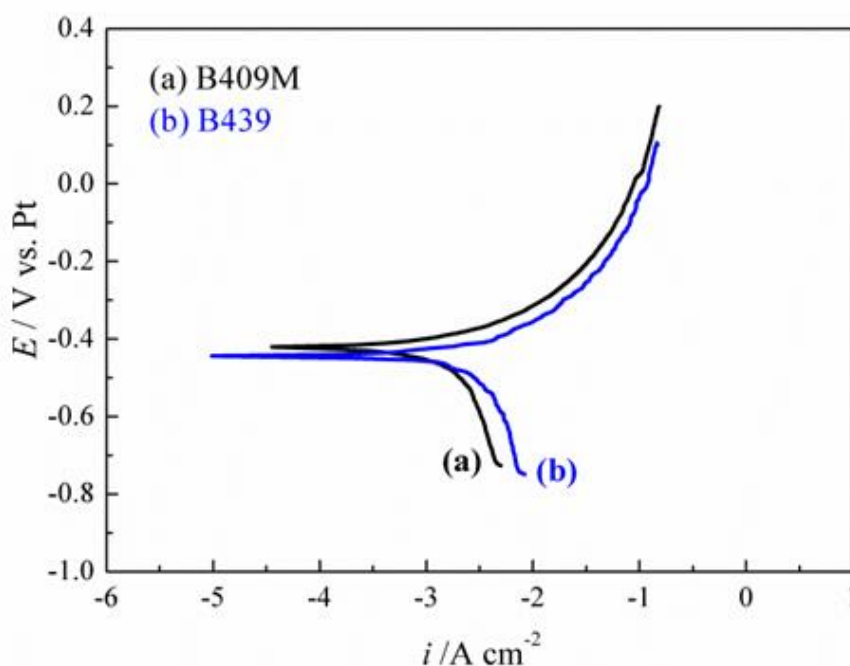


Figure 1. Potentiodynamic polarization curves of the ferritic alloys B409M and B439 at 700 °C in molten (Li,Na,K)F under a pure Ar atmosphere.

Table 2. Electrochemical parameters obtained from the Tafel linear fitting of the polarization curves for B409M and B439 in molten (Li,Na,K)F at 700 °C.

Alloy	$b_a /$ (mV·dec ⁻¹)	$b_c /$ (mV·dec ⁻¹)	$E_{corr} /$ (mV vs. Pt)	$I_{corr} /$ ($\mu\text{A}\cdot\text{cm}^{-2}$)
B409M	68.1	-57.1	-429	631
B439	34.5	-110	-432	738

3.2 Electrochemical impedance measurement

Fig. 2 illustrates the typical Bode and Nyquist plots for the corrosion of B409M and B439 in molten (Li,Na,K)F at 700 °C for 100 h. The corrosion of the alloy during the experimental duration result in similar impedance features. The Nyquist plots of both samples are composed of two capacitive loops, i.e., a very small semi-circle at high frequencies and a large semi-circle at low-frequency port. The large capacitive loop at low frequencies may indicate scale formation on the alloy surface. The semi-circle at high-frequencies during the initial immersion is not as evident in the extended immersion plots. Furthermore, the time constants in the high-frequency region for the B409M and B439 samples cannot be clearly characterized, especially in the initial stage. The impedance value for the B439 sample decreases with the exposure time, and the impedance value for B409M irregularly changed.

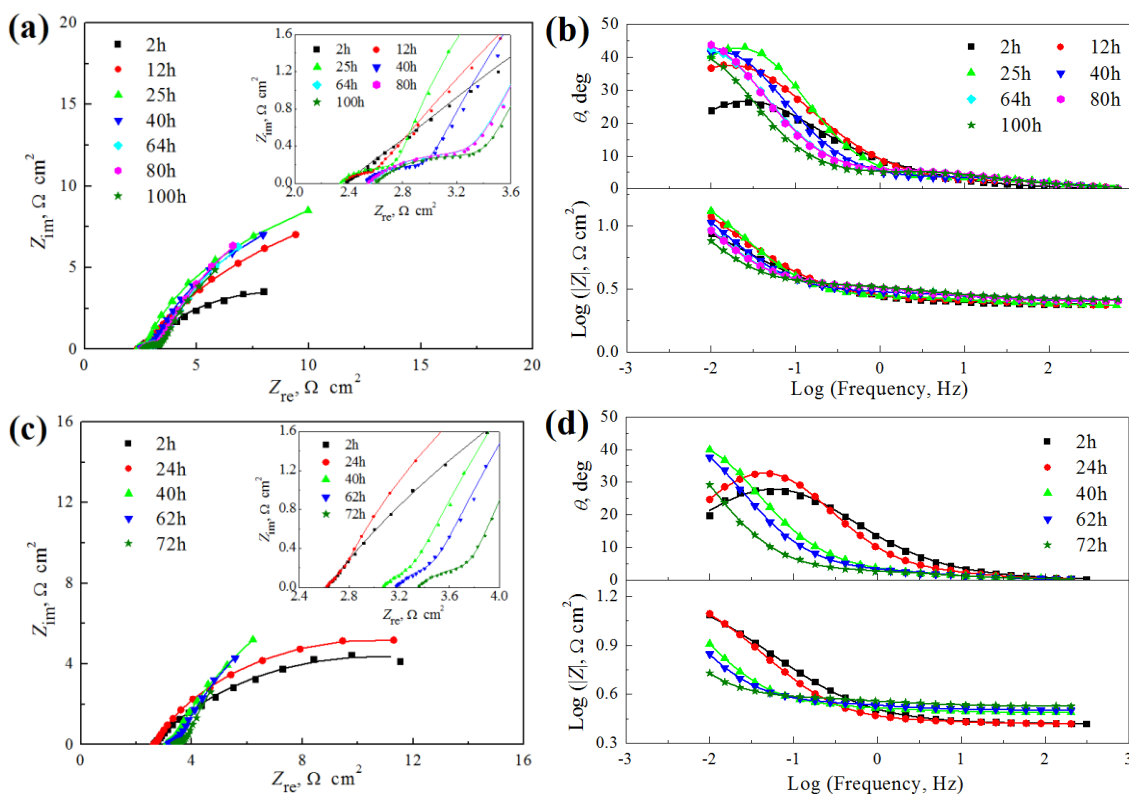


Figure 2. Bode and Nyquist plots for the corrosion of the Fe-based alloys, B409M (a) and (b) and B439 (c) and (d), in molten (Li,Na,K)F at 700 °C under a pure Ar atmosphere. Symbol: experimental data; line: simulation data.

3.3 Corrosion products

The surface morphologies of B409M and B439 after a 100 h immersion in molten (Li,Na,K)F are presented in Fig. 3. The ferritic steels, B409M and B439, both experience general corrosion and are severely eroded by molten (Li,Na,K)F. Voids formed on the surfaces of the specimens. However, the surface morphology of B439 (Fig. 3b) is rougher than that of B409M (Fig. 3a) after a 100 h immersion in molten (Li,Na,K)F. The morphology and the EDX results indicate that, Cr-rich oxides are formed on the surfaces of the B409M and B439 specimens.

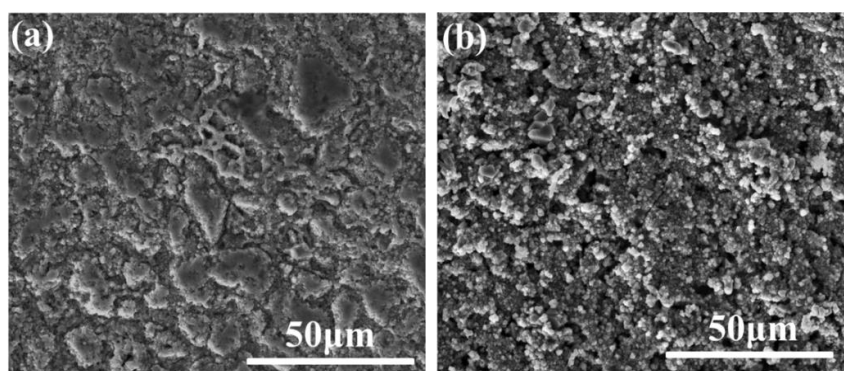


Figure 3. Surface morphologies of B409M (a) and B439 (b) after corrosion at 700 °C for 100 h in molten (Li,Na,K)F under an Ar atmosphere.

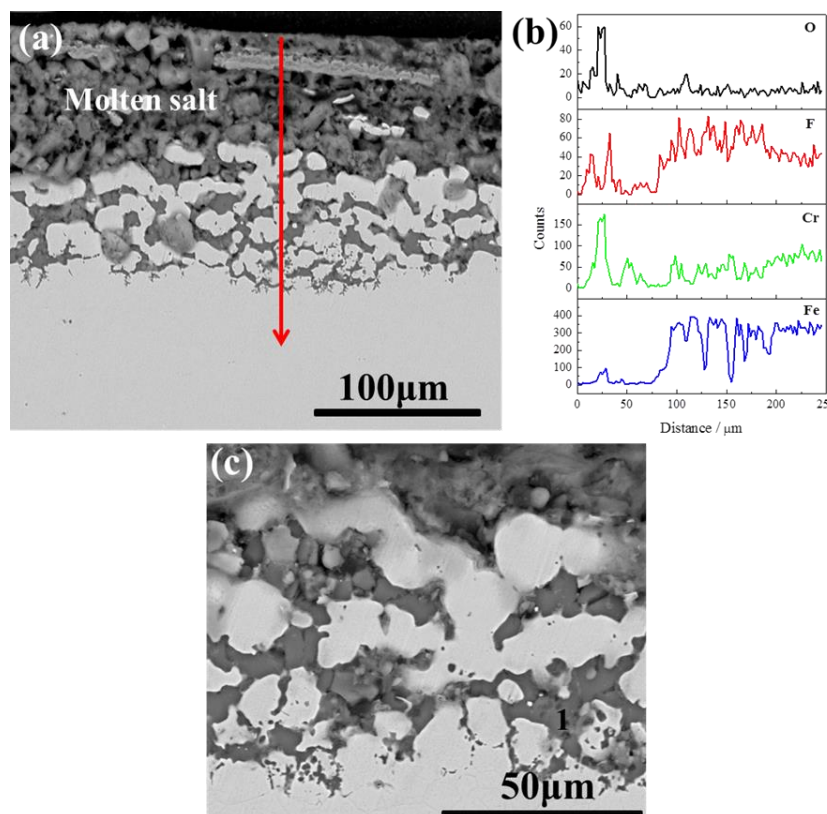


Figure 4. Cross-sectional morphologies and EDX analysis of the ferritic steel, B409M, after corrosion at 700 °C for 100 h in molten (Li,Na,K)F under an Ar atmosphere.

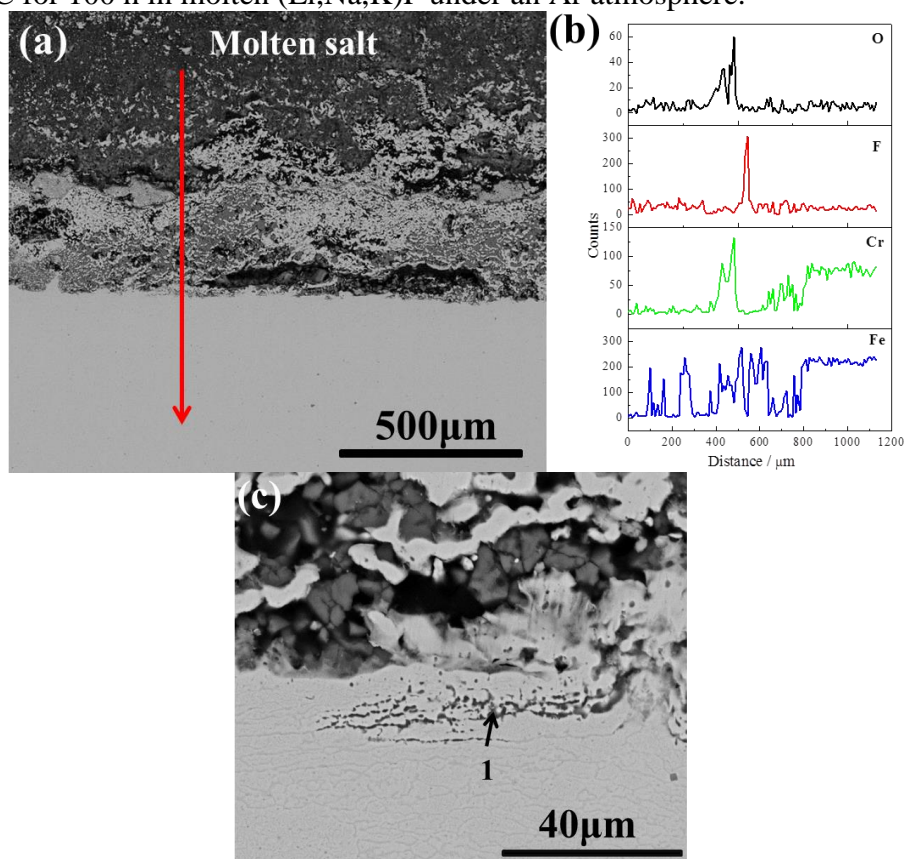


Figure 5. Cross-sectional morphologies and EDX analysis of the ferritic steels, B439, after corrosion at 700 °C for 100 h in molten (Li,Na,K)F under an Ar atmosphere.

Examination of the cross-sectional morphologies of the corroded samples by SEM and EDX indicates that a non-protective Cr-enriched scale composed of a mixture of oxides and fluorides formed on the surfaces of B409M and B439 after a 100 h immersion as shown in Fig. 4 and 5. The corrosion layer for the B439 specimen is porous, but more continuous and thicker than that on B409M. Cr-depleted zones with depths of approximately 100 μm and 600 μm are also observed for the B409M and B439 specimens due to the selective dissolution of Cr in molten (Li,Na,K)F. Furthermore, the grain boundary is preferentially corroded in both B409M and B439 (Fig. 4c and 5c). The corrosion of Cr-containing alloys in molten fluorides occurs through the dissolution of Cr. Voids filled with Cr-containing molten salt remain at the grain boundaries in the near-surface regions of B409M and B439 after a 100 h immersion in molten (Li,Na,K)F. Some Cr-containing products are observed on the surfaces of B409M and B439, and these products have a chemical composition of 8.78Cr-5.35Fe-58.54F-16.57K-10.76Na (at.%) in zone 1 of Fig. 4c and 8.14Cr-15.73Fe-50.60F-16.25K-9.28Na (at.%) in zone 1 of Fig. 5c. Furthermore, the corrosion depths of B409M and B439 are much deeper than that of ferritic steel JLF-1 (8.92Cr-2W) reported by M. Kondo[13]. This result is because KF is

hygroscopic, and the Ar flow can carry a certain concentration of water vapor; thus, HF is generated at elevated temperatures through Eq. (1):



Therefore, the initial molten (Li,Na,K)F contains a small amount of HF (several ppm), which will increase the redox potential of the melt and cause the melt be more corrosive to ferritic steels.

3.4 Interpretation of the impedance spectra

The impedance spectra for the corrosion of B409M and B439 can be fitted by the equivalent circuit in Fig. 6, where R_s represents the molten salts resistance, C_{dl} is the double-layer capacitance, C_c is the oxide capacitance, R_t is the charge transfer resistance, and R_c is the corrosion layer resistance. Considering the dispersion effect, a constant phase angle element (CPE) Q is used to replace C_{dl} and C_c in the fitting procedure. The impedance of CPE is expressed as:

$$Z_{\text{CPE}} = \frac{1}{Y_0(j\omega)^n} \quad (1)$$

Thus, the total impedance of Fig. 5 can be expressed as:

$$Z = R_s + \frac{1}{Y_c(j\omega)^{n_c} + \frac{1}{R_c + \frac{1}{Y_{dl}(j\omega)^{n_{dl}} + \frac{1}{R_t}}}} \quad (2)$$

where Y_{dl} and n_{dl} , and Y_c and n_c are the constants representing the element Q_{dl} and Q_c , respectively.

According to the equivalent circuit of Fig. 5 the impedance spectra for the corrosion of the ferritic alloys is fitted and some electrochemical parameters are listed in Tables 3-5, respectively. Fig. 2 clearly shows that the fitting results are quite good, indicating that the proposed equivalent circuit is reasonable.

Tables 3-4 present that the value of R_s for the corrosion of B409M and B439 increases with immersion time due to salt consumption and the formation of large amounts of corrosion products. Moreover, the values of n_{dl} and n_c obviously deviate of from 1. The center of the semi-circle is on the real axis provided that the double layer functions as a perfect capacitor. However, in many cases, the center of the semi-circle is not on the real axis, and the semi-circle is rotated clockwise by a certain angle around the origin. This phenomenon is called a dispersion effect. The dispersion phenomenon can be attributed to a non-uniform electric field at the electrode/solution interface due to the roughness of the electrode surface [21, 22]. In molten salt corrosion, the non-uniform electric field may be related to the roughness of the scale grown on the metal surface or the molten salt system[23, 24]. In the present study, a dispersion effect may be caused by the porous structure of the corrosion layer (Fig. 4 and 5). The values of R_t for the corrosion of the B409M and B439 specimens are similar in magnitude. For the corrosion of B409M, R_t undergoes irregular changes during the exposure time. Due to fast oxidation and fluoridation in the initial stage, a scale covers the specimen and blocks the Faradaic

current, and this is coupled with the simultaneous, well-known dissolution process of oxides and fluorides in the melt, resulting in fluctuations in R_t for B409M. However, the values of R_t for the B439 specimen have an overall upward trend. The increase in R_t is because the scale on the surface of B439 is thicker and more continuous, causing the electrochemical processes on B439 to require more energy than those on the B409M specimen. Furthermore, the values of R_t for both the B409M and B439 specimens are several times larger than the values of R_c , indicating that the transfer rate of ions, mainly chromium, through the ferritic steel to the surface is the rate-limiting process.

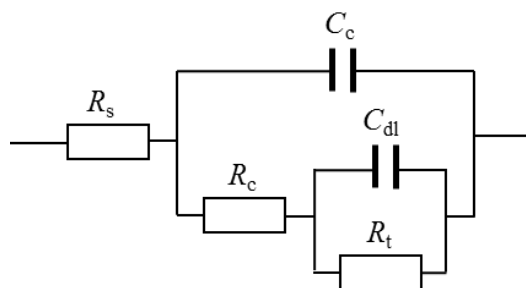


Figure 6. Equivalent circuits representing the impedance spectra for the corrosion of B409M and B439 in molten (Li,Na,K)F at 700 °C under a pure Ar atmosphere.

Table 3. Fitting results of the impedance spectra for B409M in molten (Li,Na,K)F at 700 °C.

Time (h)	R_s ($\Omega \cdot \text{cm}^2$)	Y_c ($\Omega^{-1} \cdot \text{cm}^{-2} \cdot \text{s}^{-n}$)	n_c	R_c ($\Omega \cdot \text{cm}^2$)	Y_{dl} ($\Omega^{-1} \cdot \text{cm}^{-2} \cdot \text{s}^{-n}$)	n_{dl}	R_t ($\Omega \cdot \text{cm}^2$)
2	2.39	0.4187	0.65	1.90	0.2907	0.73	10.4
6	2.38	0.3147	0.65	0.81	0.2986	0.67	20.5
12	2.36	0.04392	0.80	0.25	0.5186	0.69	30.7
18	2.38	0.03441	0.84	0.28	0.5137	0.71	30.5
25	2.31	0.1902	0.55	0.67	0.4574	0.93	36.6
30	2.49	0.07952	0.74	0.36	0.6710	0.82	16.7
40	2.51	0.1408	0.64	0.61	0.7666	0.83	27.9
50	2.55	0.1659	0.63	0.88	1.044	0.88	19.1
64	2.56	0.1701	0.63	1.02	1.014	0.85	31.7
70	2.54	0.1636	0.63	1.02	1.029	0.85	33.4
80	2.54	0.1810	0.61	1.08	1.030	0.86	38.6
100	2.60	0.1820	0.61	1.04	1.504	0.86	27.2

Table 4. Fitting results of the impedance spectra for B439 in molten (Li,Na,K)F at 700 °C.

Time (h)	R_s ($\Omega \cdot \text{cm}^2$)	Y_c ($\Omega^{-1} \cdot \text{cm}^{-2} \cdot \text{s}^{-n}$)	n_c	R_c ($\Omega \cdot \text{cm}^2$)	Y_{dl} ($\Omega^{-1} \cdot \text{cm}^{-2} \cdot \text{s}^{-n}$)	n_{dl}	R_t ($\Omega \cdot \text{cm}^2$)
2	2.63	0.02580	0.65	0.041	0.3088	0.62	16.2
12	2.68	0.1096	0.64	0.80	0.9903	0.95	12.5
24	2.62	0.3668	0.70	0.92	0.07711	0.98	15.4
30	2.84	0.3318	0.78	0.24	0.6233	0.80	22.9
40	2.08	0.4369	0.75	0.42	0.9258	0.80	31.8
50	3.15	0.5010	0.72	0.49	1.125	0.82	35.2
62	3.18	0.5143	0.72	0.51	1.250	0.82	37.9
72	3.35	0.6890	0.59	0.68	2.469	0.87	39.2
100	3.27	0.5962	0.59	0.54	1.605	0.69	37.1

3.5 Corrosion mechanism

The corrosion of B409M and B439 is mainly due to fluoridation processes. Under the present experimental conditions, H₂O impurities inevitably exist because KF is hygroscopic and deliquescent and a certain concentration of water vapor can be carried by the Ar flow. H₂O can react with the fluoride salts to generate gaseous HF. Therefore, the actual experimental conditions include a H₂O-HF-Ar system. However, under the present experimental conditions, the concentration of oxidant H₂O is only several ppm, which is not sufficient to provide the oxygen pressure required to form a protective scale on the specimens. Therefore, with the consumption of H₂O and the generation of HF, the fluorination reactions occur. Simultaneously, metal fluorides dissolution processes occur due to their solubility in molten fluoride salts [25], resulting in the porosity and non-protectiveness of the scale. Because the Cr concentration in B439 is higher than that in B409M, the corrosion layer that forms on the surface of B439 is more continuous and thicker than that on B409M (Fig. 4). The oxidation and fluoridation processes will cease or become self-limiting when the moisture and HF are consumed or the solubility limits of the transition metal fluorides in the molten fluoride salt are reached [26, 27].

The molten (Li,Na,K)F first permeates the grain boundaries where the Cr-carbides are enriched, because the Cr-carbides at the grain boundaries are more prone to attack by dissolving into molten (Li,Na,K)F. Therefore, the Cr-enriched boundaries are more strongly corroded than the normal area, which is subjected to general corrosion. Subsequently, void formation occurs in the alloys due to Cr dissolution at the surface of the exposed grains and the grain boundaries. Initially, voids form at the subsurface of the alloy through oxidation processes with H₂O impurities and the selective dissolution processes of the active elements in the alloy, primarily Cr, into the molten fluoride salt. When the surface is depleted of Cr, the Cr from the interior of the alloy diffuses down the concentration gradient to the surface. Diffusion occurs by a vacancy mechanism and is faster along the grain boundary than the grain, and an excess of vacancies build up in the near-surface regions and grain boundaries of the

alloy. Finally, the vacancies precipitate into voids and uniformly distribute along the alloy surface and grain boundaries, as shown in Fig. 4c and 5c.

4. CONCLUSIONS

The ferritic steels, B409M and B439, are both in active dissolution states at the corrosion potential in molten (Li,Na,K)F at 700 °C. The corrosion current density of B439, which has a higher Cr content, is approximately $738 \mu\text{A}\cdot\text{cm}^{-2}$, and is larger than that of B409M ($631 \mu\text{A}\cdot\text{cm}^{-2}$), which has a lower Cr content. The electrochemical impedance spectra for the corrosion of B409M and B439 during a 100 h experimental test have two capacitive loops. General corrosion and grain boundary corrosion are caused by fluoridation processes. In addition, voids form and uniformly distribute through the alloy surface and grain boundaries.

ACKNOWLEDGMENTS

This project is supported by the Bagui Scholars Program of Guangxi Autonomous Region in 2016, the Academician Workstation Building Project of Guangxi Zhuang Autonomous Region Scientific and Technological Department [Grant No. [2014] 91], and the National Natural Science Foundation of China [Grant No. 51271190].

References

1. S. Jitsukawa, A. Kimura, A. Kohyama, R.L. Klueh, A.A. Tavassoli, B. van der Schaaf, G.R. Odette, J.W. Rensman, M. Victoria and C. Petersen, *J. Nucl. Mater.*, 329(2004) 39.
2. T. Muroga, J.M. Chen, V.M. Chernov, K. Fukumoto, D.T. Hoelzer, R.J. Kurtz, T. Nagasaka, B.A. Pint, M. Satou, A. Suzuki and H. Watanabe, *J. Nucl. Mater.*, 367(2007)780.
3. A. Sagara, *Fusion Eng. Des.*, 81(2006) 2703.
4. M. Kondo, T. Nagasaka, A. Sagara, N. Noda, T. Muroga, Q. Xu, M. Nagura, A. Suzuki and T. Terai, *J. Nucl. Mater.*, 386(2009)685.
5. H. Yamanishi and A. Sagara, Annual Report of National Institute for Fusion Science (2000)177.
6. R.W. Moir, H.F. Shaw, A. Caro, L. Kaufman, J.F. Latkowski, J. Powers and P.E.A. Turchi, *Fusion Sci. Technol.*, 56(2009)632.
7. Ding Xiangbin, Sun Hua, Yu Guojun, Zhou Xingtai, *J. Chin. Soc. Corr. Pro.*, 35(2015)543.
8. Ken-ichi Fukumoto, Ryota Fujimura, Michio Yamawaki, Yuji Arita, *J. Nucl. Sci. Technol.*, 52(2015)1323.
9. Hongda Wang, Qian Feng, Zhen Wang, Haijun Zhou, Yanmei Kan, Jianbao Hu, Shaoming Dong, *J. Nucl. Mater.*, 487(2017)43.
10. M. Seregin, A. Parshin, A.Y. Kuznetsov, L. Ponomarev, S. Mel'nikov, A. Mikhalichenko, A. Rzhetskii, R. Manuilov, *Ridiochem.*, 53(2011)491.
11. D.J. Rogers, T. Yoko and G.J. Janz, *J. Chem. Eng. Data*, 27(1982)366.
12. Wei-Jen Cheng, Robert S. Sellers, Mark H. Anderson, Kumar Sridharan, Chaur-Jeng Wang, Todd R. Allen, *Nucl. Technol.*, 183(2013)248.
13. M. Kondo, T. Nagasaka, Q. Xu, T. Muroga, A. Sagara, N. Noda, D. Ninomiya, M. Nagura, A. Suzuki, T. Terai and N. Fujii, *Fusion Eng. Des.*, 84(2009)1081.

14. T. Nagasaka, M. Kondo, T. Muroga, N. Noda, A. Sagara, O. Motojima, A. Suzuki and T. Terai, *J. Nucl. Mater.*, 386(2009) 716.
15. H. Nishimura, T. Terai, M. Yamawaki, S. Tanaka, A. Sagara and O. Motojima, *J. Nucl. Mater.*, 307(2002)1355.
16. B. El-Dasher, J. Farmer, J. Ferreira, M.S. de Caro, A. Rubenchik and A. Kimura, *J. Nucl. Mater.*, 419(2011)15.
17. M. Kondo, T. Nagasaka, V. Tsisar, A. Sagara, T. Muroga, T. Watanabe, T. Oshima, Y. Yokoyama, H. Miyamoto, E. Nakamura and N. Fujii, *Fusion Eng. Des.*, 85(2010)1430.
18. J. Farmer, B. El-Dasher, M.S.d. Caro and J.Ferreira, *MRS Fall Meeting*, (2008).
19. Y.L. Wang, H.J. Liu and C.L. Zeng, *J. Fluorine Chem.*, 16(2014)1.
20. Y.X. Xu, Y.L. Wang and C.L. Zeng, *High Temp. Mat. PR-ISR*, 0(2013)1.
21. G.M. Schmid, *Electrochim. Acta*, 15 (1970) 65.
22. S. Iseki, K. Ohashi, S. Nagaura, *Electrochim. Acta*, 17 (1972) 2249.
23. C.L. Zeng, W. Wang and W.T. Wu, *Corros. Sci.*, 43(2001)787.
24. C.L. Zeng, W. Wang and W.T. Wu, *Oxid. Met.*, 53(2000)289.
25. D. Williams, L. Toth and K. Clarno, *ORNL*, (2006).
26. M. Sohal, M. Ebner, P. Sabharwall and P. Sharpe, *INL/EXT*, (2010).
27. J.R. Keiser, *ORNL*, (1977).

© 2018 The Authors. Published by ESG (www.electrochemsci.org). This article is an open access article distributed under the terms and conditions of the Creative Commons Attribution license (<http://creativecommons.org/licenses/by/4.0/>).